



HAL
open science

Laminar gypsum crust on lede stone: Microspatial characterization and laboratory acid weathering

Tim de Kock, Jeroen van Stappen, Gilles Fronteau, Marijn Boone, Wesley de Boever, Fabrice Dagrain, Geert Silversmit, Laszlo Vincze, Veerle Cnudde

► **To cite this version:**

Tim de Kock, Jeroen van Stappen, Gilles Fronteau, Marijn Boone, Wesley de Boever, et al.. Laminar gypsum crust on lede stone: Microspatial characterization and laboratory acid weathering. *Talanta*, 2017, 162, pp.193 - 202. 10.1016/j.talanta.2016.10.025 . hal-01689068

HAL Id: hal-01689068

<https://hal.science/hal-01689068>

Submitted on 23 Mar 2018

HAL is a multi-disciplinary open access archive for the deposit and dissemination of scientific research documents, whether they are published or not. The documents may come from teaching and research institutions in France or abroad, or from public or private research centers.

L'archive ouverte pluridisciplinaire **HAL**, est destinée au dépôt et à la diffusion de documents scientifiques de niveau recherche, publiés ou non, émanant des établissements d'enseignement et de recherche français ou étrangers, des laboratoires publics ou privés.

Laminar gypsum crust on Lede stone: Microspatial characterization and laboratory acid weathering

Tim De Kock^{a,b,*}, Jeroen Van Stappen^a, Gilles Fronteau^c, Marijn Boone^a, Wesley De Boever^{a,b},
Fabrice Dagrain^d, Geert Silversmit^e, Laszlo Vincze^e, Veerle Cnudde^a

a: PProGress/UGCT – Department of Geology, Ghent University, Krijgslaan 281/S8, 9000 Ghent, Belgium

b: Inspect BVBA, Technologiepark 3, 9052 Ghent-Zwijnaarde, Belgium

c: GEGENAA (EA3795), Université de Reims Champagne-Ardenne (URCA), 2 Esplanade Roland Garros, 51100 Reims, France

d: Stone Assistance sprl, Spin-Off of University of Mons, Clos des Botteresses 4, 4317 Viemme, Belgium

e: XMI - Department of Analytical Chemistry, Ghent University, Krijgslaan 281/S12, 9000 Ghent, Belgium

* Corresponding author: Tim De Kock PProGress/UGCT – Department of Geology, Ghent University, Krijgslaan 281/S8, 9000 Ghent, Belgium. E-mail addresses: tim.dekock@ugent.be, tim@inspect.rocks.

Abstract:

Gypsum crusts are typical decay forms on limestone in polluted urban environments. Their origin and relation to the stone facies have been thoroughly investigated in the past three decades. Here, we present the combined use of novel techniques for a microspatial structural, chemical and mechanical characterization of a laminar black gypsum crust on a sandy limestone. These techniques include i.a. X-ray computed microtomography, X-ray Fluorescence micromapping, permeability mapping and the scratch test. They reveal the typical architecture of a laminar gypsum crust, with an outer opaque layer, a subsurface gypsum crystallization layer and a deeper cracked zone passing irregularly into the sound stone. Gypsum crystallization is mostly restricted to an irregular outer zone with an average thickness of 500 μm , while cracks are found deeper within the rock. These cracks decrease the rock strength to more than 27.5 mm below the surface. Because of their surface parallel orientation and thickness of > 10–100 μm , they create the potential for surface scaling. This is shown by a laboratory acid test where the crack network extensively developed due to further exposure to an SO₂ environment. The use of novel techniques opens potential for the study of different decay forms and can be used for stone diagnosis with regards to conservation studies.

Keywords: Gypsum crust / X-ray computed microtomography / X-ray fluorescence mapping / Drilling resistance / Scratch test

1. Introduction

Natural building stones are known to alter their surface properties when used and exposed to atmospheric conditions as a result of the interaction between the stone and its environment. Many processes interfere with each other and the eventual alteration pattern can be complex and dynamic. Eventually, the interaction of different processes leads to different erosional or depositional alteration patterns [28]. Erosional weathering removes material from the stone by e.g. dissolution, exfoliation, flaking, scaling or sanding, while depositional weathering adds material to the stone's surface by e.g. efflorescence, encrustation, biocolonization. Both can be caused by chemical, physical and biological processes.

Of all types of alteration, gypsum crusts and more specifically gypsum crust on carbonate rocks are among the most present and the most studied (e.g. [35]). Gypsum crusts are sulfate encrustations on building stones in polluted urban environments which mainly consist of gypsum crystals, and are often called black crusts due to the incorporation of airborne dust and particulate matter [7]. Several studies were assigned to the relation between black crust formation and urban pollution (e.g. [24,25,52]). Morphologically, these crusts can have a laminar or more framboidal or dendritic structure [44], depending on the conditions under which they were formed. Their structure may be strongly related to the microfabric of the host rock [23], but in general, a gypsum crust consists of an outer opaque layer, a subsurface layer with gypsum crystallization and a deeper fractured zone irregularly passing into the sound stone [32]. Black crusts develop on rain-sheltered surfaces due to dry or wet deposition of airborne SO₂ on stone with a carbonate phase or lime mortars in the presence of water and catalyzing air pollutants [3,37,39,40]. On surfaces exposed to rain, black crusts will be washed off due to the moderate solubility of gypsum, when the rate of rain washing exceeds the rate of deposition. On more rain-protected surfaces, they have the potential to initially stabilize the stone surface [43]. Eventually, they can detach mechanically through contour scaling, where not only the crust, but also a layer of the disaggregated stone held by the crust is lost [41,46]. Detachment of the crust can occur by other processes like mechanical impact, crystallization of ice or salt behind the crust, hydration/dehydration or thermal stresses. After detachment, the process of gypsum crust formation can resume, resulting in several crusts [41], although the conditions might be different due to the legacy of the previous crust forming episode.

Accurate classification of stone weathering and diagnosis of the stone conditions is the first step for stone conservation studies [28,49]. Notwithstanding having fundamental knowledge on weathering forms, a preliminary case-study of the exact stone type and building environment is often appropriate. Therefore, several methods exist and are being developed for the effective characterization of building materials, both in the field and in the laboratory [45]. Although stone decay is observed and handled with on the macroscale, it is the expression of microstructural changes in the pore space of the building material. This paper therefore presents a microspatial structural and chemical characterization of a laminar black gypsum crust on a sandy limestone, followed by further laboratory weathering by a standard acid test. The material under investigation is Lede stone, on which black crusts were previously described [14,31]. It was stated that glauconite could play a triggering role in the sulphation process [19]. The formation of gypsum crusts on Lede stone was recently studied on the micro-scale in laboratory conditions [16,17]. In the present study, current methods as thin section microscopy and SEM-BSE and -EDX, which have typically been used for describing gypsum crusts [30,44,50], are multidisciplinary combined with advanced methods such as X-ray computed microtomography (μ CT) [10,29], X-ray fluorescence micromapping (μ XRF) [9] and the scratch test [36]. The aim is to study the chemical and physical relation between the laminar gypsum crust and the underlying sandy limestone, and to explore the benefits of these techniques for the characterization of altered rocks in laboratory, as well as for the interpretation of field tests. In addition, a laboratory weathering test comparable to Dewanckele et al. [16] was performed on these samples, to study the further effects of sulphation on the gypsum crust dynamics.

2. Materials

The material under investigation is a quartz-rich limestone from the north-western part of Belgium, known as the Lede stone or Balegem stone. It originates from the sandy deposits of the Lutetian (Eocene) Lede Formation where cementation occurred at generally 1–3 specific horizons and gave rise to discrete stone banks of several decimeters thickness. At outcrop regions, these banks occur amongst unconsolidated sediments and provided the local source of durable building material. The limestone can be classified as a quartz-rich packstone to grainstone with varying amounts of micrite matrix, microsparite cement and fossil fragments, amongst which miliolid and *Nummulites variolarius* forams. The quartz fraction has a bimodal distribution, dominantly with fine sand sized subangular grains contaminated with coarse well-rounded grains. A small part of the detritic fraction is composed of feldspars and heavy minerals. Approximately 3% glauconite is present. The Lede stone is originally greyish, but acquires a typical rust-coloured patina in buildings. The open porosity is 8.27 ± 1.09 vol% and the compressive strength is 48.4 ± 12.6 MPa [15], although there is a large spread depending on the microfacies. (e.g. [14]).

Lede stone is the most important natural building stone resource in northwestern Belgium [15] and it therefore is also prominently present in the built heritage of northern Belgium and the Netherlands. The stone is prone to sulphation, typically leading to black gypsum crusts in protected environments, and flaking or scaling crusts in surfaces exposed to water run-off. Exposed to atmospheric conditions, the stone also develops a yellow-brownish to rust-coloured patina, giving the stone an animated and aesthetically accepted touch. Whereas these are the most typical phenomena of weathering and ageing, other decay forms can occur but are related to local conditions. Some examples can be found in De Kock et al. [14]. Weathered specimens were collected at the Sint-Salvator church in Wieze (Belgium) from the well-ventilated top of the tower where they were protected from direct rain impact. In these conditions, a thin black crust developed on the stone surface (Fig. S1, Supplementary material).

3. Methods

The weathered sample was cut into sagittal sections for subsampling. The first section was impregnated with an EpoFix resin, stained with yellow fluorescent dye (EpoDye) for the preparation of subsamples for optical microscopy, SEM, μ CT and μ XRF. Optical microscopy was performed on 30 μ m thin sections using a Zeiss Axioscope A1 equipped with AxioCam and EpoDye filter. Polished sections were prepared for SEM and μ XRF studies, using an alcohol-based diamond slurry. A JEOL 5300-LV SEM was used for SEM-BSE imaging and EDX mapping. μ XRF spectra were recorded in vacuum with an EDAXEAGLE III μ -probe at the X-ray Microspectroscopy and Imaging Group (XMI, Ghent University). An area with both crust and stone material was mapped (40 kV, 11 s live time per pixel, pixel resolution ~ 100 μ m, map dimensions 9100 μ m \times 5100 μ m). The detection limit for SEMEDX is around 1000–3000 ppm, whilst for μ XRF this is tens to hundred ppm, depending on the element (e.g. Al 100 ppm, Fe 15 ppm). On the other hand, the image resolution of the SEM-EDX mapping is approximately 2.5 μ m per pixel, whilst the resolution of μ XRF mapping here is approximately 100 μ m per pixel. The sample surface, however, does not require specific coating for μ XRF measurements. Two cylindrical subsamples with diameters of 8 and 1.8 mm were cored for μ CT scanning at the Centre for X-Ray Tomography of the Ghent University (UGCT) using a custom built micro-CT setup [33]. The 8 mm sample was scanned at a tube voltage of 120 kV and a tube current of 75 μ A, and a 1 mm Al filter was used for beam hardening reduction. For the 1.8 mm sample, the tube was operated at 80 kV and a tube current of 37.5 μ A. A spatial resolution of 12.48 μ m and 2.04 μ m was obtained for each sample respectively. The μ CT images were reconstructed with the Octopus reconstruction software [47], 3D

image analysis was performed with Octopus Analysis (formerly Morpho+) [6] and the volumes were rendered using VGStudio MAX software.

The second cut section was not impregnated and was used to perform the scratch test [11,36] to assess the microspatial variation in rock strength. Successive 100 μm deep cuts were performed along the sample surface using a 94 μm wide cutter to generate a groove with a total depth up to 2750 μm . The resulting rock strength was expressed as unconfined compressive strength, and the scratch tomography image was matched with a photo of the stone section.

Six drilling tests were performed on the same sample of the second section, aligned in the same direction of the scratch test. The custombuilt drilling system [11,12] used a 5 mm drill bit and measures both torque and weight on bit versus depth as an indicator of the variation in strength. The drill bit was operated at a Rotational speed of 250 RPM and Rate of Penetration of 50 $\mu\text{m}/\text{rotation}$.

Non-destructive gas permeability measurements were performed with a TinyPerm II probe permeameter [22] on the same sample as the scratch test measurements. The measurements were performed in a grid on the sagittal section and the results were interpolated and plotted in Matlab. This plot was also matched with a photo of the stone section. However, measurement was somewhat problematic near the crustal surface because of stone instability and thus the entire section could not be covered by measurements. This area is left white within the resulting image.

A cylindrical sample with a diameter of 6 mm was cored from the non-impregnated second section. It was mounted on a sample holder with the same diameter and sleeved with a heat-shrink tubing so that only the crust was exposed on top. Similar to Dewanckele et al. [16], the sample was subjected for 21 days to an acid environment according to EN 13919 [21], further described as the 'acid test'. First, the sample was wetted and placed in the atmosphere of a closed 50 l container, containing a solution of 150 ml H₂O and 500 ml 5–6% H₂SO₃. After 21 days, the sample was removed from the container, rinsed with water and left to dry in a custom designed climatic cell whilst the sample was scanned with μCT using HECTOR [34]. The conditioning of the sample in the climatic cell was controlled by a humidity generator (GenRH Surface Measurement Systems Ltd.). The sample was scanned with μCT before the test and before drying at the end of the test. To allow a direct comparison of the μCT images before and after the test, scanning, reconstruction and analysis were performed with the same parameters for both scans. The X-ray tube was operated at 120 kV and 10 W and equipped with an 1 mm Al filter. 2401 projections of 1 s were taken over 360°. The resulting voxel size was 4.99 μm or 9.88 μm for rebinned (factor 2) images. The scans were registered using Dataviewer software from Bruker MicroCT and analysis was performed with Octopus Analysis [6] using the same parameters for both scans.

4. Results

4.1. 2D structure

The laminar gypsum crust on the Lede stone from the Sint-Salvator church has been analyzed with different techniques, accordingly or complementary to Larbi et al. [31] and Dewanckele et al. [16,17], to evaluate its decay and the implications on stone conservation. Fig. 1 shows thin section micrographs at different magnifications of the Lede stone from the Sint-Salvator church with a laminar gypsum crust on the left side. The porosity of Fig. 1A in the same field of view can be more easily observed in green on the fluorescence image (Fig. 1B). In general, the crust exists of three layers: an opaque layer (zone 1), a subsurface layer with gypsum crystals (zone 2), and a deeper cracked layer which passes into the sound stone (zone 3). This can be best observed in a higher magnification (Fig. 1C). The opaque layer

is thin (tens of microns) and irregular. It consists of loosely bound opaque and iron-rich particles, adherent to the surface. Underneath, there is a zone which is cemented by very fine gypsum crystals. Its thickness is variable, but mainly fluctuates around 500 μm . It encompasses autochthonous quartz grains and patches of calcite. Larger bioclasts such as *Nummulites variolarius* show a positive relief with respect to the rest of the unweathered stone. Specifically for these bioclasts, weathering starts with dissolution of the fibrous carbonate cement lining of the object, followed by partial dissolution of the calcite test (i.e. the shell) layer per layer (Fig. S2A, Supplementary material). It is remarkable that a substantial amount of the glauconite has a brown discolouration. This is especially true for glauconite grains within the gypsum crust or adjacent to the underlying crack network. This discolouration is due to atmospheric weathering, releasing free iron that subsequently can precipitate as amorphous iron oxide, ferrihydrite or goethite.

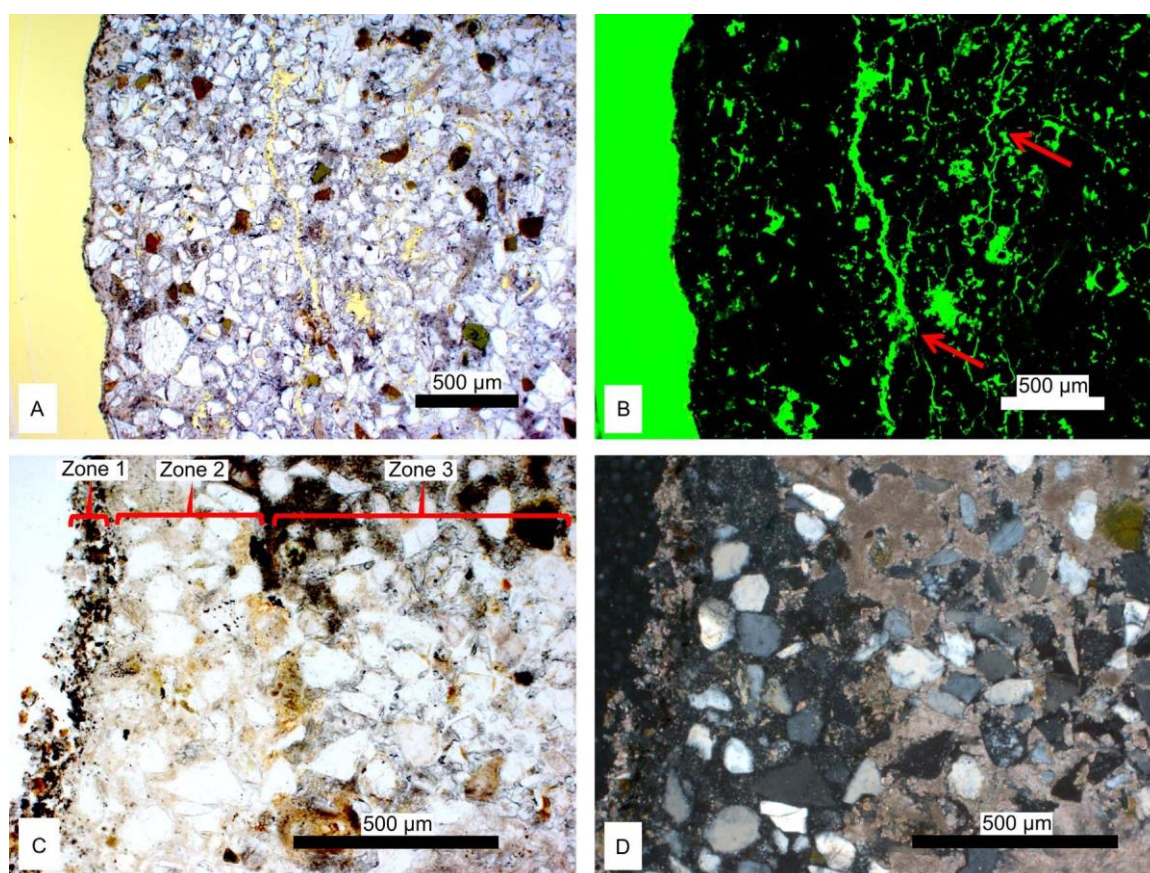


Fig. 1. (A) thin sections micrograph of gypsum crust; (B) fluorescent image of the same view as A, illustrating the porosity and fractures in green; (C) indication of opaque upper layer (zone 1), gypsum crystallization layer (zone 2) and sound stone with fractures (zone 3); (D) same field of view as (C) under crossed polars. Scale bars are 500 μm . (For interpretation of the references to color in this figure legend, the reader is referred to the web version of this article.)

Looking at the porosity distribution on the fluorescence image of Fig. 1B, a zone of lower porosity can be seen up to approximately 500 μm deep below the surface. This corresponds with the formerly described zone 2. Behind this low porosity zone, a number of surface parallel cracks exist over a depth of several hundred of microns. The crack network protrudes deeper inside the stone than the gypsum alteration does. However, using SEM, gypsum crystals were sometimes found within these cracks. The

crack network is preferentially accommodated by some textural features such as the lining of coarse quartz grains and bioclasts. Small cracks initiate at the interface of the coarse

well-rounded quartz grains and the surrounding cement or matrix. Cracks also form through the axial plane of the planispiral forams *N. variolarius* (Fig. S2A Supplementary material). The major crack network develops where these features are aligned and smaller cracks are connected.

The same structure can also be observed on SEM-BSE images in Fig. 2A. In the opaque layer of zone 1 (Fig. 2B), fly ash can be recognized both as smooth and rough spherical particles of 5–10 μm diameter. Airborne silt-sized quartz particles are also present. Zone 2 consists of densely intertwined acicular gypsum crystals, within the micrometer scale. In zone 3, cracks can be observed, sometimes with gypsum crystallization inside.

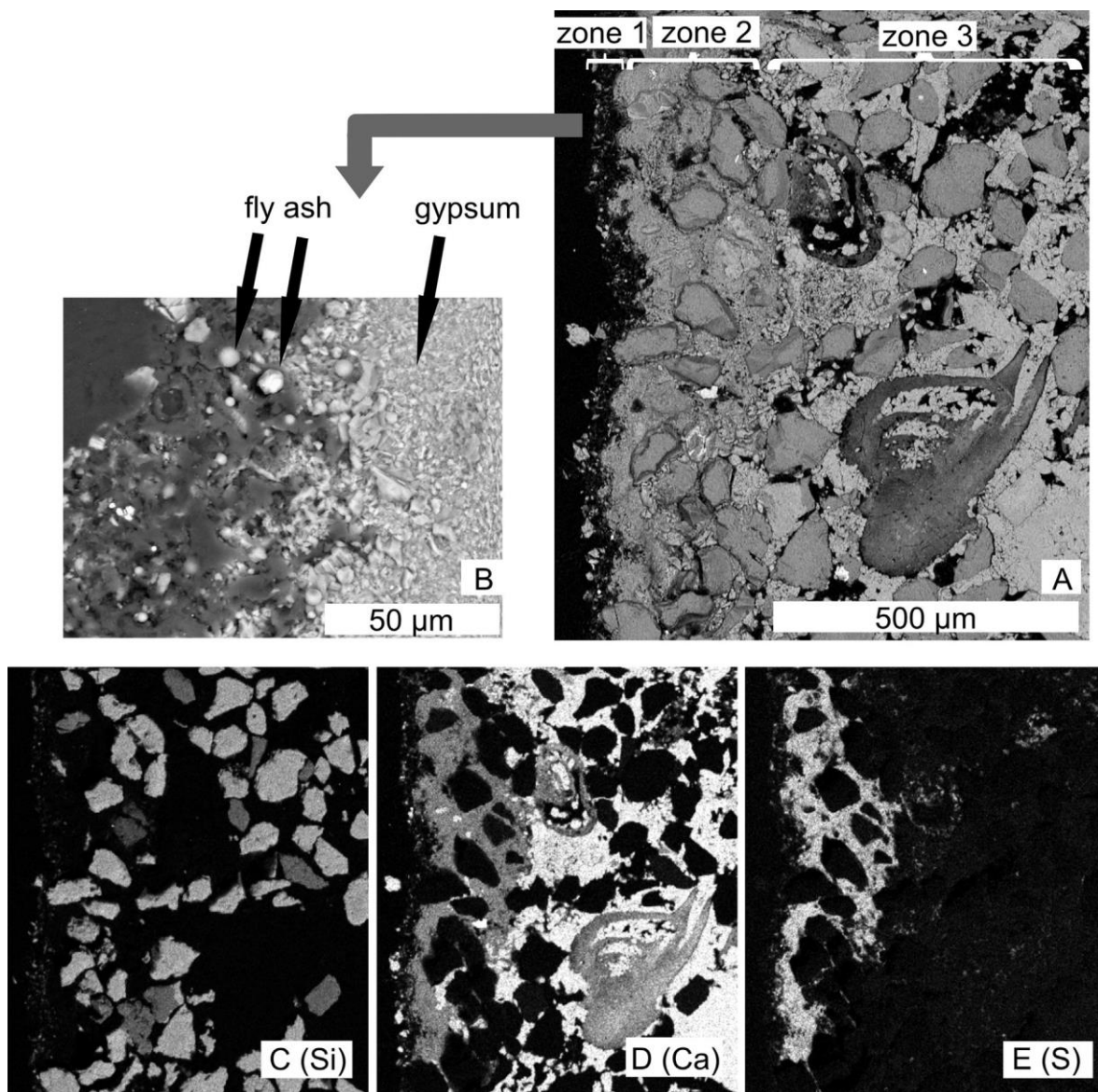


Fig. 2. (A) SEM-BSE image of gypsum crust oriented to the left with indication of zone 1, 2 and 3; (B) detailed SEM-BSE image of the crust with particulate matter in the outer layer and intertwined gypsum crystals underneath; (C-E) SEM-EDX mapping of Si, S, Ca with the same field of view as (A).

4.2. 2D composition

SEM-EDX mapping and point spectrum measurements were performed to provide more chemical information on the decay pattern (Fig. 2C–E). The crustal structure is reflected in the elemental maps. On the Si map (Fig. 2C), quartz and feldspar grains are visible. Feldspars could be recognized by spotting them in a K map, but can be differentiated here from quartz by the number of counts for Si in the EDX images. Quartz grains are bright, feldspars are more grey. The Ca map (Fig. 2D) displays the calcite cement and matrix on the right side of the sample together with the Ca-tests of miliolid forams. To the left, there is a Ca signal with lower number of counts. This correlates well to the S map (Fig. 2E) and corresponds to the gypsum crust as observed in thin section. Finally, the signal of phosphorus and iron was too low to be detected in SEM-EDX mapping.

Laboratory μ XRF mapping shows the spatial occurrence of Al, Si, P, S, K, Ca, Fe and Zr in relative concentrations, with the crustal surface oriented to the left (Fig. 3). Here especially, the increased content of P and Fe in the crust is detected. Six main hotspots of Si can be recognized, representing the fraction of coarse well-rounded quartz grains. On the other hand, the Ca hotspots are related to bioclasts. Over the rest of the area, pixels show a combined Si and Ca signal, because the sampling depth of μ XRF and the resolution ($\sim 100 \mu\text{m}$) is too low to resolve very fine quartz fraction ($< 125 \mu\text{m}$) from the calcite matrix and cement. The hotspots in Al, K and Fe are related to feldspar grains (K, Al and possibly Ca), and glauconite (K, Al, Fe). The elemental maps show a clear elevation in P and S content in the crust compared to the bulk of the stone, with S indication the crystallization of gypsum. The phosphor enrichment in the crust was not noticed in SEM-EDX.

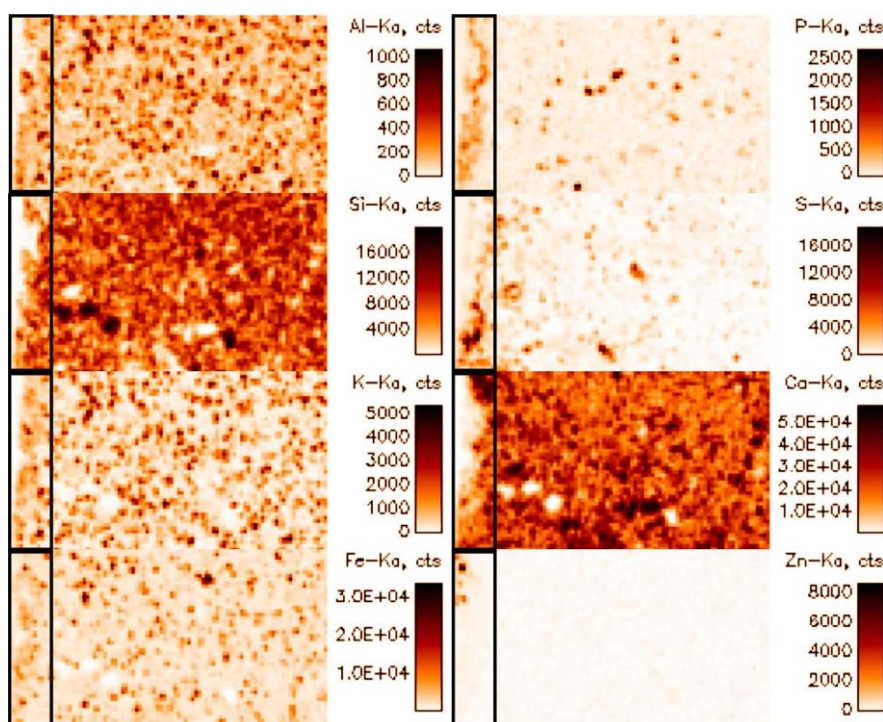


Fig. 3. μ XRF mapping of cross section of 5.1 mm x 9.1 mm, crustal surface oriented on the left side and marked by rectangle, with relative concentrations per element of Al, P, Si, K, Ca, Fe and Zn spectra. Fe and K enrichments in the crust are less clear, and lack true hotspots. However, the relative concentration is higher for the crust than for the bulk of the sample, hotspots excluded.

4.3. 3D structure

Finally, the sample was analyzed in 3D using μ CT. Fig. 4 shows a sagittal μ CT slice through the cylindrical subsample of 1.8 mm, with the gypsum crust oriented to the top. μ CT has the advantage of analyzing and rendering the sample in both 2D and 3D, providing a numerous stack of slices (several hundreds) which each represent a different section of the total 3D volume. The results show that μ CT is well suited for the microstructural investigation of the laminar gypsum crust.

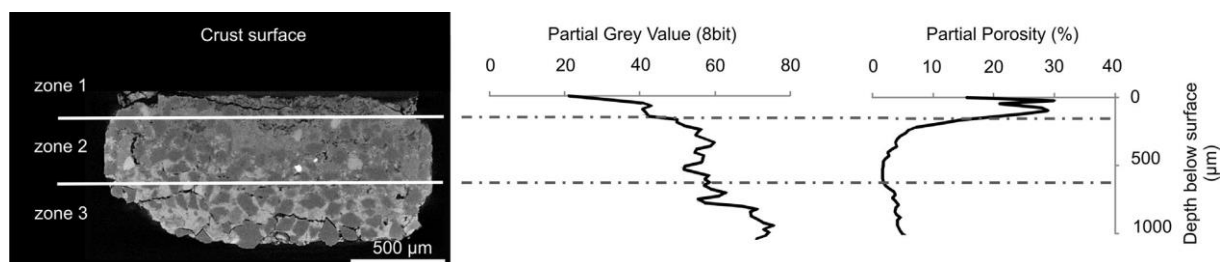


Fig. 4. Sagittal slice obtained with μ CT and correlated Partial Grey Volume and Partial Porosity graphs of the total volume in function of depth beneath the crustal surface.

Fig. 4 represents a 2D sagittal section through the 3D volume in an 8 bit greyscale image. Black represents pore, whilst the various grey values are material. At a specific X-ray energy, the lower the effective atomic number and density of a material, the darker it appears in the image, and vice versa. The dark grains are mainly quartz and some minor amounts of feldspar or, a little brighter, glauconite. The lightest cement phase in the bottom of the sample is calcite, whilst the darker cement on top is gypsum. The same three zones as observed in thin sections can also be recognized in this sagittal slice and are marked as such on the image. A frontal slice of the three zones is presented in Fig. S3 (Supplementary material). The Partial Grey Value (PGV) and Partial Porosity (PP) are calculated on the 3D volume from top to bottom (Fig. 4). Whilst PP is dependent on the segmented porosity only, the PGV also reflects the average grey value of the material. Thus PGV is dependent on the amount of porosity as well as the phases present. In both PGV and PP, the three zones are distinguishable when their values are plotted in function of depth beneath the crustal surface (Fig. 4). Based on this and the visual observations, the three zones are arbitrary marked on the image. Although they are separated by straight lines for simplification and correlation between the image and the graphs, it should be clear that the real boundary between each zone is irregular. It can be seen that zone 1, the opaque layer, is loosely bound, resulting in a very high PP and thus low PGV. The difference with the underlying zone 2 is remarkable. This zone has a much lower porosity with a minimum around 500 μ m below the surface. The PGV shows a plateau for this zone, allowing to delimit its extension. This plateau is caused by a uniform zone of low porosity consisting mainly out of quartz grains in a gypsum matrix. Underneath, zone 3 is differentiated by higher PGV and a slightly higher porosity. Gypsum crystallization is almost nonexistent in this zone and calcite remains chemically unaffected. The average porosity of this zone is similar to normal values for similar fresh stone samples [15]. Peaks in porosity are both caused by natural variability within the fabric and the occurrence of small cracks. The preparation of longer cores, although imbedded in resin, was problematic. Most likely, this was the result of a larger crack being present at the irregular base of the sample seen in Fig. 4.

Very specific features can be observed in some of the various 2D reconstructed μ CT slices. Zone 2 is less thick where larger bioclasts are present. The coarser bioclasts are known to stand in positive

relief upon weathering. In this case, it can be seen that *N. variolarius* specimens are less prone to weathering than the surrounding calcite components, similar to the thin section observations. Nevertheless, weathering is protruding from the outer edge into the test layers along the perforate hyaline calcite (Fig. S2B, Supplementary material). Where calcite is dissolved, gypsum subsequently precipitates. Also axial cracks are formed within these planispiral forams. Glauconite within the gypsum crystallization zone is intensely cracked and corroded, so that released parts could disintegrate completely.

The cracks were segmented in 3D, using a multiscale Hessian crack filtering [48] to select elongated features that belong to porosity. After this segmentation, the cracks were separated from the elongated primary pores by manual selection in Octopus Analysis. Once the cracks were isolated, they were separated into objects using the Octopus Analysis tool based on a watershed separation. The resulting objects were regarded as individual cracks, together building the crack network. It is possible to calculate the maximum opening (MO), i.e. diameter of the largest sphere that fits within the object, and the object orientation in 3D. Fig. 5 displays the 3D rendering of the cylindrical samples and the location of the cracks within the transparent volume. In the 1.8 mm cylinder, many cracks exist very near to the surface.

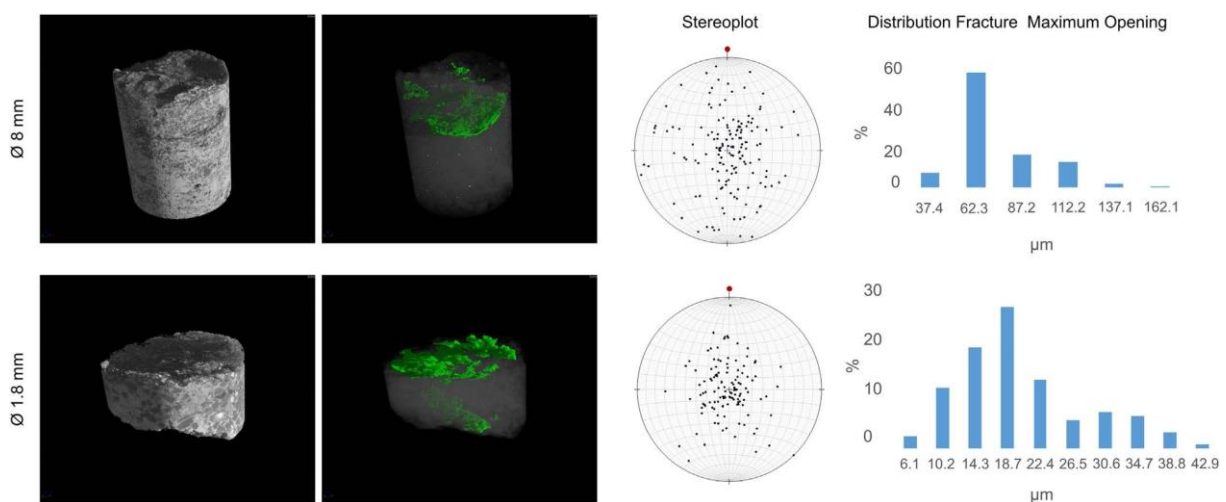


Fig. 5. 3D rendering of μ CT samples (left) with transparent volume and fractures depicted in green (right); stereoplot of fracture orientation and distribution of the fracture Maximum Opening (right). (For interpretation of the references to color in this figure legend, the reader is referred to the web version of this article.)

They are found within the opaque layer and on the boundary with the zone below. Also, the smaller cracks at the bottom, which were observed in Fig. 4, are clearly connected to the border, when rendered in 3D. They are most likely part of a larger crack network, which caused the sample to crack during coring. Thus, the bottom surface can be seen as a larger crack, but could not be analyzed quantitatively. The segmented cracks have a MO which is distributed around 20 μ m.

In the 8 mm sample, smaller cracks are also present near the surface, but the largest crack network runs approximately 2.5 mm below the surface. The pole of the crack is plotted on stereographic projections. A plot in the centre of the projection thus represents an object with its long axis oriented parallel to the stone surface (i.e. crustal surface). The majority of the cracks plot around the centre and thus run (sub-)parallel to the stone surface (Fig. 5). Some cracks, however, clearly have an inclined

orientation. This second generation of cracks forms the connection steps between the first generation, individual and sub-parallel cracks. The MO of these cracks is distributed around 60 μm , but can grow larger than 100 μm , which is quite substantial on the scale of observations. As only objects with MO three times the spatial resolution were included in the analysis, the small cracks as observed in the 1.8 mm sample were not included in the analysis of the 8 mm sample. It is thus the intention to combine the information of both separate analysis.

4.4. Petrophysical properties

Understanding the petrophysical properties of weathering forms is important to estimate stone surface stability and to decide on interventions and stone treatments. Here, this was addressed by measuring unconfined compressive strength and gas permeability. The stone section on which the analysis was performed is given in Fig. S4 (Supplementary material). The scratch test was performed in the outer 27.5 mm of the stone surface (Fig. S4B, Supplementary material). Red and yellow represent the strongest parts of the rock, with compressive strengths up to 150 MPa, which are not unusual for this type of rock. The dark to light blue represents strengths from tens of MPa to around 50 MPa. There is an important decreasing gradient in strength in the outer few centimeters, as a result of the superficial stone decay. Drilling resistance profiles (Fig. S5, Supplementary material) show more detail of this weaker zone. Drops in weight on bit illustrate the passage through weaker zones while peaks are stronger zones. The larger drops at 8 mm depth in drilling resistance profile 6 and at 2 mm depth at drilling resistance profile 1 are the result of major cracks. The decayed zone is the thinnest in drilling resistance 4, where the stone strength increases at a depth of 5 mm. It can be correlated to the position where the scratch test reaches its highest strength values. This means that initial rock strength corresponds to an average weight on bit of around 20 N, whilst lower weights are measured in the decayed zone, as is most clear in profiles 1, 3 and 5. The measurements again show that the decayed part has an irregular thickness. After performing the scratch test, part of the crust (top left in Fig. S4A, Supplementary material) broke off during the cutting of the sample, preparing it for gas permeability measurements. This crack correlates with an area of weakness observable in the scratch test tomography and to the drop in weight on bit at a depth of 8 mm in profile 6. Therefore, unfortunately, gas permeability measurements could not be obtained for the entire cross section. In addition, permeability very near to the crustal surface was too high to obtain representative measurements with this method. However, the mapping does show some interesting features (Fig. S4C, Supplementary material). The core of the sample demonstrates relatively low gas permeability, scaled in blue, with values ranging from 98 to 240 mD. Within this bulk, there is a zone of slightly higher permeability represented in light blue. This could be due to variation within the stone fabric. Towards the remainder of the crust, permeability starts to increase strongly up to 679 mD, with highest permeability correlating to a thick zone of relative weakness observed in the scratch test tomography.

4.5. Acid weathering of black gypsum crust

Fig. 6 shows a sagittal cross-section of the sample with μCT before (initial state) and after the test (final state), with the exposed crust on the top. The sample has undergone dimensional changes, prohibiting an easy registration of the scans. As the dimensional changes, which include a rotation and translation of the grains, are more pronounced in the top part, the bottom part of the scans were used to register both volumes. The obtained transformation parameters were then applied to register the entire volume of the final state to the initial state. Subsequently, both volumes were cylindrically cropped to eliminate the irregularity of the lateral edges and the heat-shrink tubing in the analysis.

Fig. S6 (Supplementary material) shows the 8-bit grey value histogram of the initial and final state. The voxels that represent porosity have grey values of 30–40, quartz and feldspar grains have grey values of 85–105, gypsum has grey values of 105–115 and calcite has grey values of 115–130. Voxels on the interface between two phases have an average value depending on the relative weight of each phase in the voxel (partial volume effect). The histogram of the initial state shows a peak in the quartz interval and a positive skew for the grey values related to calcite. In the final state, after 21 days of acid weathering, this positive skewness has decreased and the peak has increased. This indicates a relative decrease of calcite compared to the initial state. The increase in the peak can be interpreted as a result of different effects, firstly the increase in gypsum, and secondly to an increase in the surface/volume ratio of the porosity (i.e. different kind of porosity) which results in an increase of partial volume effect around the carbonate and gypsum phase.

On Fig. 6, it can be seen that the volume of the final state has increased at the top of the sample. This can also be observed when plotting the amount of voxels that represent the sample in function of depth for both the initial and final state (Fig. S7, Supplementary material). This graph can also be seen as a representation of the largest volumetric cross section of the sample with the top directed to the left. It shows that the volume has expanded $\pm 200 \mu\text{m}$ in the topwards direction.

Fig. 6 also gives a visual impression of the changes within the sample. In the final state, three differences are remarkable compared to the initial state. First, a new compact and thin crust developed on top of the initial crust. Secondly, a zone with intensive cracking developed just beneath the initial crust. And finally, the bulk of the sample is less porous. This is shown in Fig. S7B (Supplementary material) where the partial porosity is plotted in function of depth beneath the crust. The initial state can be interpreted the same way as in Section 4.3. However, because of the lower resolution, zone 1 and 2 cannot be distinguished clearly. Rather, only the transition of zone 1 and 2 to zone 3 is visible at around $750 \mu\text{m}$ depth. The partial porosity has changed drastically in the final state. Whilst the porosity of the top part increased almost 5 times, the porosity in the deeper parts decreased by a factor 2.

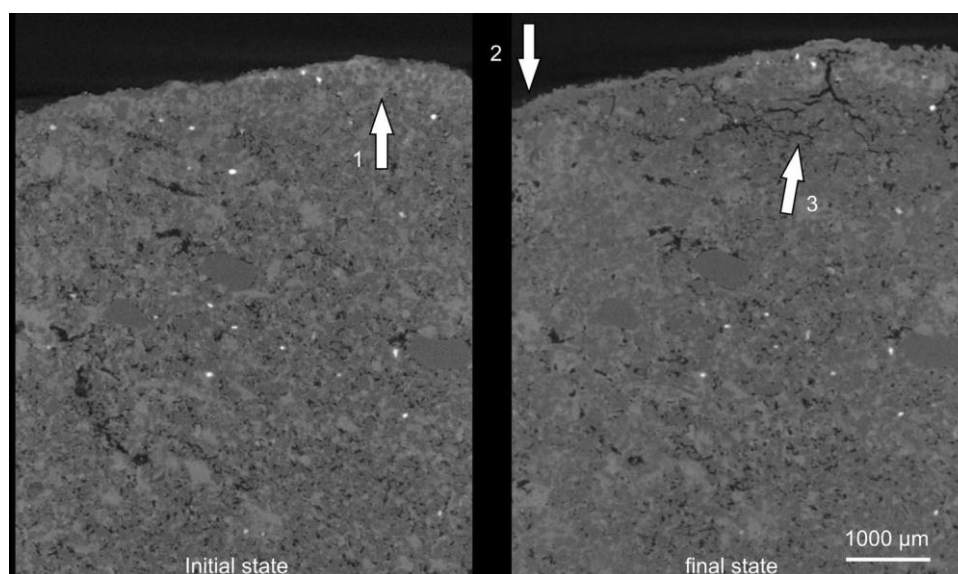


Fig. 6. Sagittal cross section of μCT with the crust on top of the initial state (left) and the final state (right). Arrow 1 indicates the depth of the original gypsum crust. Arrow 2 indicates superficial gypsum crystallization crust after 21 days acid exposure. Arrow 3 indicates a zone with a development of cracks. Relative grey scale given in the histogram of Fig. S5 (Supplementary material).

The increase in porosity can be attributed to dissolution and the development of cracks in a zone up to 1500 μm depth (Fig. 6). These cracks form a network subparallel (horizontal) and oblique (vertical) to the surface. They mainly develop in the zone just below the initial gypsum crust. On the other hand, the decrease in porosity in the deeper

parts of the stone can mainly be attributed to precipitation in the pore network. To illustrate this, Fig. S8 (Supplementary material) shows a detail of the top part of the sample (top) together with a zonal model (bottom). Here it can be seen that a newly crystallized crust covers the entire top of the sample. Underneath, the initial gypsum crust remains largely unaffected, except for some cracks accommodating the underlying cracked zone and connecting it to the outside. As these cracks are covered with the new crystallization, they developed pre- or contemporary to the crystallization on the top.

Fig. S9 (Supplementary material) shows a slice through the top, with the original crust on the initial state image (top) and the evolution of this crust in the final state (bottom). The crust clearly increased in volume. The tracking of dense particles near the border of the original crust can be used to evaluate the growth direction of the crust. Doing so, it can be seen that the gypsum crust has grown in two directions. In some locations, the crust grew outwards, as a result of crystallization on the top (also visible in Fig. S8, Supplementary material). Other grains indicate the inwards progression of the crust, as they become incorporated in the gypsum crust in the final state. Over the entire sample, the crust grew inwards, by dissolution of the calcite cement and the precipitation of gypsum. Underneath this superficial crystallization, the crack network is visible in planar view (subparallel to the crustal surface). Here, the crack network tends to form a more polygonal network. The cracks observed here, mainly correspond to the vertical cracks in Fig. S8 (Supplementary material).

5. Discussion

Black gypsum crusts drastically change the aesthetic appearance of architecture and sculptures by black discolouration and modification of surface finishing and details. Furthermore, they are only a dominant visual expression of several interacting decay processes combining crystallization, dissolution, cracking and bio-colonization, leading to heavy damages on the stone superficial surface, e.g. scaling and flaking. In this study, we looked at the morphology of laminar black gypsum crust which covers the entire stone surface and how this relates to the stone's microstructure. The combination of several spatial characterization techniques allowed the identification of different structural and compositional elements of the crust and the altered stone below. Their spatial distribution allowed for an understanding of how these mechanisms are related to each other and how they are involved in surface stability and strength.

5.1. Microstructure

The observed layered structure of the black gypsum crust is consistent with the observations of Maravelaki-Kalaitzaki & Biscontin [32]. There is a clear contribution of particulate matter and other airborne dust on the surface of the crust, which can best be studied under the SEM microscope. μCT images, on the other hand illustrate the nature of these particles; irregularly adherent to the outer surface on which they are deposited. Gypsum alteration, however, occurs underneath this zone where calcite crystals are dissolved by sulphurous acid solutions and provide Ca^{2+} ions. This process preferentially exploits finer crystal phases as these have higher specific surface [17,23]. Therefore, calcite dissolution is mainly restricted to the finer calcite matrix and cement. Gypsum does not necessarily crystallize on locations where calcite was dissolved. In moist rocks, the pore fluids enriched in atmospheric sulphur and autochthonous calcium will migrate through the pore system towards the

exterior in case of drying or towards the interior in case of exterior wetting. Salts, and thus gypsum, crystallize by heterogeneous nucleation out of a supersaturated solution [42]. In rocks, there are sufficient nuclei available, yet still phases with high specific surface have higher chance to act as nucleus [17]. On the other hand, crystals form in supersaturated solutions, which can be obtained by drying. When crystallization is induced by drying, gypsum will accumulate at the evaporation front, near the surface and subsurface of the stone [8]. This explains the occurrence of the gypsum layer, zone 2, near the stone surface with a discontinuous thickness of approximately 500 μm , very similar to the observations made by Beck and Al-Mukhtar [5] on tuffeau limestone. It can be assumed that this zone grows from the interior outwards by crystallization of gypsum at the interface with the stone. For the same reason, gypsum crystallization can be observed at crack surfaces deeper within the stone. Beck and Al-Mukhtar [5] made similar observations on tuffeau limestone, where they measured a thickness of 0.5 mm for the real gypsum crust, but a thickness of 20 mm for the altered stone.

5.2. Cracks

μCT facilitated the 3D characterization of the orientation and maximum opening of the crack network. Most are oriented (sub-) parallel to the surface. The cracks can grow to more than 100 μm wide, several millimeters below the surface, initiating the detachment of the crust by scaling as observed by Smith et al. [41]. The cracks originate near the rounded coarse quartz grains, where initial circumgranular porosity is present. Thus, the presence of these grains can be seen as a flaw. They are further facilitated by the axial plane of *N. variolarius* and by the easily weathered glauconite grains. Dewanckele et al. [16] observed the initiation of micro-cracks due to the sulphation process underneath the gypsum crust. Dreesen et al. [18] found such (sub-) parallel cracks in Lede stone at depths of 5–25 mm and designated them as frost cracks. Cracks at depths of 5–25 mm are in accordance with the observations of the scratch test and the drilling test, which is reflected by a decrease in strength. The thickness of the weaker layer is variable, but reaches more than 27.5 mm near the stone edges. This exceeds by far the average thickness of 500 μm of the gypsum alteration zone, but rather corresponds to the zone where cracks are present. This cracking might be enhanced or facilitated by progressive discrimination between the deeper stone and the crystallization zone, where porosity is altered and water flow might be redirected parallel to the surface [4]. In turn, cracks increase the permeability and reduce rock strength. This will have a positive feedback on the partial dissolution of carbonates within the deeper altered rock and the further propagation of micro-cracks induced by gypsum crystallization pressure. It will also affect the local water saturation which influences freeze-thaw weathering. Such increase in permeability is confirmed by the gas permeability mapping, which suggests an increased permeability near the stone surface. However, only a small part near the stone surface could be accurately measured and more tests on permeability variation within the decayed zone should be done on other samples.

5.3. Glauconite

The glauconite grains in the decayed zone show physical disintegration and a brownish discolouration. This could be the result of acid-induced release of Al, Fe and Mg from the crystal lattice [26] when glauconite comes in contact with sulphurous pore waters. This results in wedge-like splitting, which facilitates cracks and further physical disintegration. In contrast to the suggestion of Dreesen et al. [18], there is no evidence here of glauconite acting as favourable nucleation site for gypsum crystallization. The released iron can precipitate locally, causing the brownish discolouration of the grains. On the other hand, these are a possible source of the relative iron enrichment in the crust as observed by μXRF mapping. The potassium enrichment, which is observed in this way, could also be related to the iron released from glauconite grains. This superficial iron enrichment can be related to

the brown-coloured patina, which is typical for Lede stone [14,15]. Gas permeability mapping suggests an increased permeability near the stone surface, improving the capability of pore water to interact with the glauconite grains, and most likely related to the crack network and dissolution of the calcite matrix and cement.

5.4. Phosphorous

Finally, a phosphorous enrichment in the crust was observed in the μ XRF sample, but not in the SEM-EDX samples. Designation of phosphorous phases in crusts on building materials can be troublesome [2]. Different authors have described the potential role of historical treatments [13], organic contributions [27] or atmospheric pollution [51] on phosphates present on building stone surfaces. In this study, the information is insufficient to determine the origin of the phosphorous unambiguously. However, given the sample was provided from the church tower, bird droppings are the most probable source. This would also explain its presence in the μ XRF mapping and its absence in SEM-EDX images, as bird droppings vary locally.

5.5. Black crust formation

From the cross sections and the plots of the voxel volume of interest and partial porosity, it can be seen that the sample has undergone some dimensional changes as a result of local dissolution and precipitation. The histogram suggests that calcite has been dissolved and that probably gypsum precipitated. The plots indicate an outwards extension of the sample.

The dissolution of calcite took mainly place in the zone underneath the original gypsum crust. Crystallization, on the other hand, took place in the pore network of the deeper stone and on the top of the sample. Here, it crystallized both on top of the older crust, as well as underneath, thereby including non-reactive grains of the stone in the crust.

Very striking is the development of cracks underneath the original and newly formed crust. This zone is situated close to the surface, between two parts where crystallization occurred: the top crust and the deeper stone. As such, the development of these cracks could be related either to differential length changes induced by gypsum crystallization, either by drying induced tension. Differential length change can be caused by crystallization of gypsum at the top and in the deeper parts of the stone. Crystallization causing an accretion at the surface, could induce tensile stresses in the substrate. Later crystallization in the deeper parts of the stone could induce shear stresses at the base of the overlying layer, which was already cracked.

Alternatively, during the period of falling drying rate, the largest pores empty first which can cause local stress [38]. In unweathered conditions, this is insufficient to crack Lede stone. However, it is not clear how much this cracked zone was weakened by dissolution during the experiment. It is not unlikely that the same process is responsible for the cracks observed in Section 5.1 (e.g. Fig. 5), though on a different scale and with different intensities. Dreesen et al. [18] attributed similar cracks in Lede stone to frost action. However, given the good frost resistance as shown by the technical tests for this stone [15] and the observations in this experiment which did not involve freeze-thaw cycling, also the sulphation process itself could be responsible for cracking. Yet, if sulphation initiates the formation of this crack network, this will have a positive feedback on other processes such as freeze-thaw weathering which can enhance the initiated cracking.

6. Conclusion

The combination of several techniques allows a microspatial characterization of the gypsum crust. Optical microscopy and SEM are powerful investigation tools for the study of stone weathering. μ XRF can provide additional information on the spatial distribution and the relative concentration of different elements and was in this case particularly helpful in identifying a weak enrichment of Fe in the crustal surface. μ CT allows for 3D structural characterization, such as crustal thickness, cracked stone thickness, crack orientation and crack maximum opening. Scaling of the gypsum crust is caused by a crack network parallel to the surface which extends several millimeters in depth below the superficial gypsum crystallization. The scratch test provides a spatial characterization of surface strength and illustrates that superficial strength can be reduced more than 27.5 mm below the stone surface. This is the result of preferential dissolution of the calcite matrix and cement and the development of a crack network facilitated by elongated features such as circumgranular porosity or the axial plane of planar fossils. The microspatial characterization can be used for the interpretation of drilling tests in the field to assess the stone condition for further conservation studies.

As evidenced by the acid weathering experiments, the origin of the cracks can possibly solely be assigned to the sulphation process, rather than freeze-thaw action. Once originated, however, they potentially initiate a positive feedback with respect to freeze-thaw weathering. Such cracks eventually lead to the flaking or scaling of the crust. With decreasing SO₂ emissions over the last decades (e.g. [1,20]), this implies a positive outlook on the future weathering and deterioration of Lede stone and similar sandy limestones in monuments.

Acknowledgements

The special research fund of Ghent University is acknowledged for granting the research fund of Wesley De Boever. The post-doc grant of Dr. G. Silversmit was granted by the Research Foundation - Flanders (FWO). Maarten Van Landeghem of Bressers Architectenbureau is acknowledged for providing the stone specimen from the Sint-Salvator church. BOF, project UG_2832369580, JPI-JHEP project KISADAMA and FWO Research Grant 1521815N are acknowledged for contribution in the funding of the GenRH equipment for environmental control add-on modules on the X-ray CT set-ups.

Appendix A. Supplementary material

Supplementary data associated with this article can be found in the online version at doi:10.1016/j.talanta.2016.10.025.

References

- [1] L. Aguilante, A. Rodrigo, A. Avila, Long-term effects of changing atmospheric pollution on throughfall, bulk deposition and streamwaters in a Mediterranean forest, *Sci. Total Environ.* 544 (2016) 919–928. <http://dx.doi.org/10.1016/j.scitotenv.2015.12.017>.
- [2] C. Alves, Scanning electron microscopy studies of neoformations on stony materials of modern building works, *Microsc. Micro.* 19 (2013) 1241–1247. <http://dx.doi.org/10.1017/S1431927613012701>.
- [3] P. Ausset, M. Del Monte, R.A. Lefèvre, Embryonic sulphated black crust in Atmospheric Simulation Chamber and in the field: role of the carbonaceous fly ash, *Atmos. Environ.* 33 (1999) 1525–1534. [http://dx.doi.org/10.1016/S13522310\(98\)00399-9](http://dx.doi.org/10.1016/S13522310(98)00399-9).
- [4] K. Beck, M. Al-Mukhtar, O. Rozenbaum, M. Rautureau, Characterization, water transfer properties and deterioration in tuffeau: building material in the Loire valley - France, *Build. Environ.* 38 (2003) 1151–1162. [http://dx.doi.org/10.1016/S0360-1323\(03\)00074-x](http://dx.doi.org/10.1016/S0360-1323(03)00074-x).

- [5] K. Beck, M. Al-Mukhtar, Weathering effects in an urban environment: a case study of tuffeau, a French porous limestone, *Limestone in the Built Environment: Present-Day Challenges for the Preservation of the Past* 331, Geological Society Special Publications, London, 2010, pp. 103–111. <http://dx.doi.org/10.1144/SP331.8>.
- [6] L. Brabant, J. Vlassenbroeck, Y. De Witte, V. Cnudde, M.N. Boone, J. Dewanckele, L. Van Hoorebeke, Three-dimensional analysis of high-resolution X-ray computed tomography data with morpho+, *Microsc. Micro.* 17 (2011) 252–263. <http://dx.doi.org/10.1017/s1431927610094389>.
- [7] D. Camuffo, M. Delmonte, C. Sabbioni, Origin and growth mechanisms of the sulfated crusts on urban limestone, *Water Air Soil Pollut.* 19 (1983) 351–359.
- [8] A.E. Charola, J. Puhlinger, M. Steiger, Gypsum: a review of its role in the deterioration of building materials, *Environ. Geol* 52 (2007), 2007, pp. 207–220. <http://dx.doi.org/10.1007/s00254-006-0566-9>.
- [9] V. Cnudde, G. Silversmit, M. Boone, J. Dewanckele, B. De Samber, T. Schoonjans, D. Van Loo, Y. De Witte, M. Elburg, L. Vincze, L. Van Hoorebeke, P. Jacobs, Multidisciplinary characterization of a sandstone surface crust, *Sci. Total Environ.* 407 (2009) 5417–5427.
- [10] V. Cnudde, M.N. Boone, High-resolution X-ray computed tomography in geosciences: a review of the current technology and applications, *Earth-Sci. Rev.* 123 (2013) 1–17. <http://dx.doi.org/10.1016/j.scitotenv.2009.06.040>.
- [11] F. Dagrain, T. Descamps, B. Poot, Less-destructive testing of masonry materials – a comparison between scratching and drilling approaches, in: *Proceedings of the 8th International Masonry Conference, Dresden, 2010*, pp. 10.
- [12] F. Dagrain, J.C. Scaillet, S. Modestou, I. Ioannou, Evaluation of the effectiveness of masonry consolidation treatments based on scratching tomography, *Am. J. Civ. Eng. Arch.* 7 (2013) 556–574.
- [13] M.A. de Buergo, R.F. Gonzalez, Protective patinas applied on stony facades of historical buildings in the past, *Constr. Build. Mater.* 17 (2003) 83–89. [http://dx.doi.org/10.1016/S0950-0618\(02\)00107-1](http://dx.doi.org/10.1016/S0950-0618(02)00107-1).
- [14] T. De Kock, J. Dewanckele, M.A. Boone, G. De Schutter, P. Jacobs, V. Cnudde, Replacement stones for lede stone in Belgian historical monuments, *Stone in Historic Buildings: Characterization and Performance* 39, Geological Society Special Publications, London, 2014, pp. 31–46. <http://dx.doi.org/10.1144/SP391.9>.
- [15] T. De Kock, M.A. Boone, J. Dewanckele, M. De Ceukelaire, V. Cnudde, Lede stone: a potential “Global Heritage Stone Resource” from Belgium, *Episodes* 38 (2015) 91–96 (doi:).
- [16] J. Dewanckele, T. De Kock, M.A. Boone, V. Cnudde, L. Brabant, M.N. Boone, G. Fronteau, L. Van Hoorebeke, P. Jacobs, 4D imaging and quantification of pore structure modifications inside natural building stones by means of high resolution X-ray CT, *Sci. Total Environ.* 416 (2012) 436–448. <http://dx.doi.org/10.1016/j.scitotenv.2011.11.018>.
- [17] J. Dewanckele, M.A. Boone, T. De Kock, W. De Boever, L. Brabant, M.N. Boone, G. Fronteau, J. Dils, L. Van Hoorebeke, P. Jacobs, V. Cnudde, Holistic approach of pre-existing flaws on the decay of two limestones, *Sci. Total Environ.* 447 (2013) 403–414. <http://dx.doi.org/10.1016/j.scitotenv.2012.12.094>.
- [18] R. Dreesen, P. Nielsen, D. Lagrou, Provenance, durability and damage analysis of natural building stones by means of petrographical techniques, in: S.K. Kourkoulis (Ed.) *Fracture and Failure of Natural Building Stones: application in the restoration of ancient monuments, Hellas, Greece, 2006*, pp. 471–485. http://dx.doi.org/10.1007/978-1-4020-5077-0_29.
- [19] R. Dreesen, P. Nielsen, On the triggering role of glauconite in the sulphate attack of sandy limestones, based on a study of historical building stones in Flanders, Belgium, in: B. Middendorf, A. Just, D. Klein, A. Glaubitt, J. Simon (Eds.), *Proceedings of the 12th Euroseminar on Microscopy Applied to Building Materials, Technische Universität Dortmund, Dortmund, 2009*, pp. 13–19.
- [20] R. Dreesen, V. Cnudde, M. Dusar, M. De Ceukelaire, D. Bossiroy, E. Groessens, J. Elsen, T. De Kock, J. Dewanckele, In het voetspoor van Camerman: de opmars van de Franse steen in België, in: R.P.J. Van Hees, H. De Clercq, W.J. Quist (Eds.), *Stenen van Binnen, Stenen van Buiten: Natuursteen in de Jonge Bouwkunst, Delft Digital Press, Delft, 2012*, pp. 33–63.
- [21] EN 13919, Natural stone test methods – Determination of resistance to ageing by SO₂ action in the presence of humidity, 2003.
- [22] C.M. Filomena, J. Hornung, H. Stollhofen, Assessing accuracy of gas-driven permeability measurements: a comparative study of diverse Hassler-cell and probe permeameter devices, *Solid Earth* 5 (2014) 1–11. <http://dx.doi.org/10.5194/se-51-2014>.

- [23] G. Fronteau, C. Thomachot-Schneider, E. Chopin, V. Barbin, D. Mouze, A. Pascal, Black-crust growth and interaction with underlying limestone microfacies, in: R. Prikryl, Á. Török (Eds.), *Natural Stone Resources for Historical Monuments* 333, Geological Society Special Publications, London, 2010, pp. 25–34. <http://dx.doi.org/10.1144/SP333.3>.
- [24] N. Ghedini, C. Sabbioni, M. Pantani, Thermal analysis in cultural heritage safeguard: an application, *Thermochim. Acta* 406 (2003) 105–113. [http://dx.doi.org/10.1016/S0040-6031\(03\)00224-7](http://dx.doi.org/10.1016/S0040-6031(03)00224-7).
- [25] C.M. Grossi, P. Brimblecombe, I. Harris, Predicting long term freeze-thaw risks on Europe built heritage and archaeological sites in a changing climate, *Sci. Total Environ.* 377 (2007) 273–281. <http://dx.doi.org/10.1016/j.scitotenv.2007.02.014>.
- [26] M.S. Hassan, H.M. Baioumy, Structural and chemical alteration of glauconite under progressive acid treatment, *Clays Clay Min.* 54 (2006) 491–499. <http://dx.doi.org/10.1346/ccmn.2006.0540410>.
- [27] T. Hossono, E. Uchida, C. Suda, A. Ueno, T. Nakagawa, Salt weathering of sandstone at the Ankor monuments, Cambodia: identification of the origins of salts using sulfur and strontium isotopes, *J. Archaeol. Sci.* 33 (2006) 1541–1551. <http://dx.doi.org/10.1016/j.jas.2006.01.018>.
- [28] ICOMOS, Illustrated glossary on stone deterioration patterns. World Wide Web Address: (<http://www.cicrp.fr/docs/icomos-iscs-glossary.pdf>), 2008.
- [29] R.A. Ketcham, W.D. Carlson, Acquisition, optimization and interpretation of X-ray computed tomographic imagery: applications to the geosciences, *Comput. Geosci.* 27 (2001) 381–400.
- [30] J. Kim, C.H. Lee, R.H. Kim, E.J. Shin, Characterization of white and black deposits on the surface of Korean stone cultural heritages, *Microsc. Micro.* 19 (2013) 167–171. [http://dx.doi.org/10.1016/s0098-3004\(00\)00116-3](http://dx.doi.org/10.1016/s0098-3004(00)00116-3).
- [31] J.A. Larbi, R.P.J. van Hees, S. Naldini, Microscopic study of weathering of white Flemish stone from the monumental Church of Our Lady in Breda, The Netherlands, *Heron* 48 (2003) 207–219.
- [32] P. Marvelaki-Kalaitzaki, G. Biscontin, Origin, characteristics and morphology of weathering crusts on Istria stone in Venice, *Atmos. Environ.* 33 (1999) 1699–1709. [http://dx.doi.org/10.1016/S1352-2310\(98\)00263-5](http://dx.doi.org/10.1016/S1352-2310(98)00263-5).
- [33] B.C. Masschaele, V. Cnudde, M. Dierick, P. Jacobs, L. Van Hoorebeke, J. Vlassenbroeck, UGCT: new x-ray radiography and tomography facility, *Nucl. Instrum. Methods Phys. Res. Sect. A* 580 (2007) 266–269. <http://dx.doi.org/10.1016/j.nima.2007.05.099>.
- [34] B. Masschaele, M. Dierick, D. Van Loo, M.N. Boone, L. Brabant, E. Pauwels, V. Cnudde, L. Van Hoorebeke, HECTOR: a 240 kV micro-CT setup optimized for research, *J. Phys.: Conf. Ser.* (2013) 463. <http://dx.doi.org/10.1088/1742-6596/463/1/012012>.
- [35] C. Ricci, C. Miliani, B.G. Brunetti, A. Sgamellotti, Non-invasive identification of surface materials on marble artifacts with fiber optic mid-FRIR reflectance spectroscopy, *Talanta* 69 (2006) 1221–1226. <http://dx.doi.org/10.1016/j.talanta.2005.12.054>.
- [36] T. Richard, F. Dagrain, E. Poyol, E. Detournay, Rock strength determination from scratch tests, *Eng. Geol.* 147 (2012) 91–100. <http://dx.doi.org/10.1016/j.enggeo.2012.07.011>.
- [37] C. Rodriguez-Navarro, E. Sebastian, Role of particulate matter from vehicle exhaust on porous building stones (limestone) sulfation, *Sci. Total Environ.* 187 (1996) 79–91. [http://dx.doi.org/10.1016/0048-9697\(96\)05124-8](http://dx.doi.org/10.1016/0048-9697(96)05124-8).
- [38] G. Scherer, Theory of drying, *J. Am. Ceram.* 73 (1990) 3–14. <http://dx.doi.org/10.1111/j.1151-2916.1990.tb05082.x>.
- [39] C. Sabbioni, Contribution of atmospheric deposition to the formation of damage layer, *Sci. Total Environ.* 167 (1995) 49–55. [http://dx.doi.org/10.1016/00489697\(95\)04568-L](http://dx.doi.org/10.1016/00489697(95)04568-L).
- [40] S. Siegesmund, Á. Török, A. Hupers, C. Muller, W. Klemm, Mineralogical, geochemical and microfabric evidences of gypsum crusts: a case study from Budapest, *Environ. Geol.* 52 (2007) 369–381. <http://dx.doi.org/10.1007/s00254006-0588-3>.
- [41] B.J. Smith, Á. Török, J. McAllister, Y. Megarry, Observations on the factors influencing stability of building stones following contour scaling: a case study of oolitic limestones from Budapest, Hungary, *Build. Environ.* 38 (2003) 1173–1183. [http://dx.doi.org/10.1016/s0360-1323\(03\)00076-3](http://dx.doi.org/10.1016/s0360-1323(03)00076-3).
- [42] M. Steiger, Crystal growth in porous materials - I: the crystallization pressure of large crystals, *J. Cryst. Growth* 282 (2005) 455–469. <http://dx.doi.org/10.1016/j.jcrysgro.2005.05.007>.

- [43] Á. Török, Surface strength and mineralogy of weathering crusts on limestone buildings in Budapest, *Build. Environ.* 38 (2003) 1185–1192. [http://dx.doi.org/ 10.1016/S0360-1323\(03\)00072-6](http://dx.doi.org/10.1016/S0360-1323(03)00072-6).
- [44] Á. Török, N. Rozgonyi, Morphology and mineralogy of weathering crusts on highly porous oolitic limestones, a case study from Budapest, *Environ. Geol.* 46 (2004) 333–349. <http://dx.doi.org/10.1007/s00254-004-1036-x>.
- [45] A. Török, R. Přikryl, Current methods and future trends in testing, durability analyses and provenance studies of natural stones used in historical monuments, *Eng. Geol.* 115 (2010) 139–142. <http://dx.doi.org/10.1016/j.enggeo.2010.07.003>.
- [46] V. Vergès-Belmin, Pseudomorphism of gypsum after calcite, a new textural feature accounting for the marble sulphation mechanism, *Atmos. Environ.* 28 (1994) 295–304. [http://dx.doi.org/10.1016/1352-2310\(94\)90104-X](http://dx.doi.org/10.1016/1352-2310(94)90104-X).
- [47] J. Vlassenbroeck, M. Dierick, B. Masschaele, V. Cnudde, L. Van Hoorebeke, P. Jacobs, Software tools for quantification of X-ray microtomography, *Nucl. Instrum. Methods Phys. Res. Sect. A* 580 (2007) 442–445. [http://dx.doi.org/ 10.1016/j.nima.2007.05.073](http://dx.doi.org/10.1016/j.nima.2007.05.073).
- [48] M. Voorn, U. Exner, A. Rath, Multiscale Hessian fracture filtering for the enhancement and segmentation of narrow fractures in 3D image data, *Comput. Geosci.* 57 (2013) 44–53. <http://dx.doi.org/10.1016/j.cageo.2013.03.006>.
- [49] P.A. Warke, J.M. Curran, A.V. Turkington, B.J. Smith, Condition assessment for building stone conservation: a staging system approach, *Build. Environ.* 38 (2003) 1113–1123. [http://dx.doi.org/10.1016/s0360-1323\(03\)00085-4](http://dx.doi.org/10.1016/s0360-1323(03)00085-4).
- [50] J. Weber, S. Beseler, K. Sterflinger, Thin-section microscopy of decayed crystalline marble from the garden sculptures of Schoenbrunn Palace in Vienna, *Mater. Charact.* 58 (2007) 1042–1051. <http://dx.doi.org/10.1016/j.matchar.2007.04.014>.
- [51] F.G. Xu, J. Tang, S.X. Gao, Characterization and origin of weathering crusts on Kylin carved-stone, Kylin countryside, Nanjing – A case study, *J. Cult. Herit.* 11 (2010) 228–232. <http://dx.doi.org/10.1016/j.culher.2009.11.006>.
- [52] G. Zappia, C. Sabbioni, C. Riontino, G. Gobbi, O. Favoni, Exposure tests of building materials in urban atmosphere, *Sci. Total Environ.* 224 (1998) 235–244. [http:// dx.doi.org/10.1016/s0048-9697\(98\)00359-3](http://dx.doi.org/10.1016/s0048-9697(98)00359-3).